


# Bistatic Synthetic Aperture Radar With Undersampling for Terahertz 2-D Near-Field Imaging

Li Ding, Yangyang Ye, Guoyao Ye, Xiwang Wang, and Yiming Zhu 

**Abstract**—To avoid the difficult transceiver-isolation problem of a monostatic synthetic aperture radar (SAR) for terahertz (THz) near-field azimuth-range imaging, a compact bistatic SAR geometry is demonstrated in this paper. The system consists of one fixed transmitter, one moving echo receiver and one fixed direct-wave receiver. The transmitter emits wideband signals for range resolution, and the echo receiver moves along a designed trajectory for the cross-range resolution, and the direct-wave receiver is taken as a reference for synchronization. Since the wavelength of THz is in the order of millimeter or submillimeter, the requirement on subwavelength interval of spatial sampling by the Nyquist theory aggravates the measurement difficulty. To break this limitation, a compressed sensing-based imaging algorithm is presented. Allowing the undersampling both in spatial domain and frequency domain, the proposed algorithm can provide high-resolution performance with few measurements. Thus, the balance between the resolution and the amount of measurements can be made. The system geometry and imaging performance are then demonstrated by both the simulations and the experiments in the 0.178–0.188 THz band.

**Index Terms**—Bistatic synthetic aperture radar (SAR), compressed sensing, near-field imaging, synchronization, terahertz (THz) imaging.

## I. INTRODUCTION

**T**ERAHERTZ (THz), occupying a frequency interval from 0.1 to 10 THz (3 mm–30  $\mu$ m wavelength), has a great potential for the development of a high-resolution imaging system [1]–[4]. Currently, one of the most popular approaches in developing THz imagers is the synthetic aperture radar (SAR)

technique [5]–[8]. Considering the practically technical maturity and the system-establishment simplicity, plenty of SAR-based THz imagers work in a monostatic mode. No matter how many transceivers the systems utilize, their inherent property is monostatic, where the transceiver isolation is one of the key factors constraining the imaging performance. Therefore, to allow the use of antennas with more widely separation for greater isolation, bistatic and even multistatic techniques nowadays have gained increasing attentions for the THz imaging field [9]–[11].

Different from the monostatic SAR, the bistatic SAR (BiSAR) can enjoy some degrees of freedom in choosing transmitter and receiver motion trajectories [12]–[14]. Conventionally this kind of radar has used “illuminators of opportunity,” which may be either the existing radars (cooperative or noncooperative) or other designed transmissions. The receiving system of the passive nature is considered as an advantage not only from a vulnerability point of view, but also with respect to the reduced size, weight, cost, etc. Motivated by those potential advantages, bistatic configurations applied into the THz band have open up new possibilities, and some applications have been reported recently [10], [15]–[17]. A bistatic inverse SAR configuration using a THz quantum cascade laser as the transmitter and a pair of Schottky diode mixers as the receiver and reference channels, respectively, is proposed in [15] to acquire the high-resolution images of a rotated target in azimuth and elevation. For the imaging method, a bistatic fast-factorized back-projection algorithm based on quasi-monostatic mapping technique is presented in [16] to achieve far-field imaging over a large field of view. **However, to the best of our knowledge, less BiSAR demonstration exists for THz near-field imaging applications.**

This paper aims at adopting a compact BiSAR geometry to achieve azimuth-range imaging in the THz near field. The concerned BiSAR system consists of one transmitter, one echo receiver, and one direct-wave receiver. Specifically, the transmitter is fixed to emit wideband continuous waveforms, e.g., stepped-frequency (SF) signals. The echo receiver moves along a linear motion trajectory, whereas the direct-wave receiver is fixed as a reference. Such that the motion of the echo-receiver contributes to the cross-range resolution by synthetic aperture technique, and the transmitted wideband signal contributes to the range resolution. To reduce the system cost and complexity, the heterodyne- and in-phase receivers are used. Assuming that two receivers are synchronized with each other, the synchronization problem between the noncooperative transmitter

Manuscript received August 22, 2017; revised October 23, 2017 and November 27, 2017; accepted December 11, 2017. Date of publication January 9, 2018; date of current version March 1, 2018. This work was supported in part by the National Program on Key Basic Research Project of China (973 Program) (2014CB339806), in part by the Major National Development Project of Scientific Instrument and Equipment (2012YQ15009205, 2016YFC1202505), in part by the National Natural Science Foundation of China (61605113), in part by the Natural Science Foundation of Shanghai (16ZR1423100), in part by the Shanghai Leading Talent (2016019), and in part by the Young Yangtze River Scholar. (Corresponding author: Yiming Zhu.)

L. Ding and Y. Zhu are with the Terahertz Technology Innovation Research Institute and the Shanghai Key Laboratory of Modern Optical System, University of Shanghai for Science and Technology, Shanghai 200093, China, and also with the Terahertz Science Cooperative Innovation Center, Shanghai 200093, China (e-mail: sunnyding@usst.edu.cn; ymzhu@usst.edu.cn).

Y. Ye, G. Ye, and X. Wang are with the Terahertz Technology Innovation Research Institute, University of Shanghai for Science and Technology, Shanghai 200093, China (e-mail: usstyeah@163.com; yg\_usst@163.com; usst\_wsx@163.com).

Color versions of one or more of the figures in this paper are available online at <http://ieeexplore.ieee.org>.

Digital Object Identifier 10.1109/TTHZ.2017.2787465

and receivers can be solved depending on the strong coherence between the echo and the direct wave [18]. That is, following the preprocess of Hilbert transform to convert both the real echo and the real direct wave to their complex forms, the synchronization can be achieved in a mathematical way by taking the direct wave as a matched filter. After that, a near-field approximation based on Taylor-series expansion and the method of stationary phase is utilized to decompose the bistatic round-trip distance. This makes the scattered field separable for the cross-range and range directions, and a 2-D analytical expression for bistatic near-field imaging is thus obtained in the wavenumber domain.

With respect to the imaging method, the conventional Fourier transform (FT) based algorithms can be applied to both the bistatic and the monostatic system in the far- or near-field conditions [3], [5], [8]. But, the requirement of the Nyquist theory on densely sampling both in frequency domain and spatial domain aggravates the cost of system as well as the signal-acquisition time. This situation, hence, is intensified in the THz band. Shorter wavelength of THz wave makes the sampling frequency grow rapidly in the cross-range dimension and leaves little space for each sampling step. Likewise, the increased bandwidth for high range resolution also scales up the amount of measurements in the frequency domain. This motivates the development of effective imaging approach that requires only a sparse subset of frequencies and spatial samples instead of their full sets. Recently, the theory of compressive sensing (CS) has demonstrated the accurate signal reconstruction from measurements of extremely few but randomly chosen samples [19], and has received much attention in radar imaging, remote sensing, and other fields [20]–[22]. Inspired by CS, in this paper, an  $l_1$ -norm-based sparse reconstruction is exploited to achieve THz BiSAR 2-D imaging through an iterative way. Undersampling is allowed in both domains to speed up the measurement and to reduce the amounts of measurement data. Thus, the balance between the resolutions and the amount of measurements can be made. The system geometry and imaging performance are then demonstrated by both the simulations and the experiments in the 0.178–0.188 THz band.

Section II provides the details of the proposed BiSAR geometry for THz near-field imaging. A signal model of the THz BiSAR for range and cross-range imaging is constructed in detail in conjunction with the signal synchronization solution. Section III discusses the establishment of iterative sparse reconstruction based on CS theory. In Section IV, both the simulations and experiments are conducted to investigate the imaging scheme and the performance of imaging method. In Section V, some conclusions are given to summarize the main results of this paper.

## II. MODEL OF THz BiSAR

Much work has been performed in the THz imaging system to develop efficient methods to take full advantage of THz waves. This paper contributes to this field in which we consider a practicable BiSAR geometry for THz near-field imaging, and integrally demonstrate the effectiveness of synchronization and

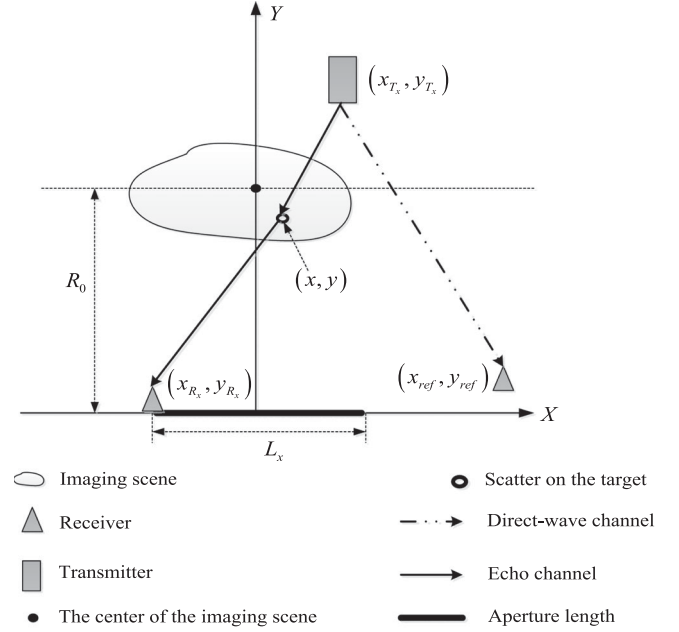


Fig. 1. Geometry of THz BiSAR for near-field imaging.

the feasibility of high-performance imaging with undersampling by the CS theory.

### A. Bistatic Geometry

For THz near-field imaging in the azimuth-range plane, the concerned BiSAR system is shown in Fig. 1. The transmitter is denoted as TX and the receiver is denoted as RX for short. They are located in a short range from the target so that the spherical wavefront is nonnegligible.

The TX is fixed at position  $(x_{tx}, y_{tx})$ , a general scatterer on the target is at position  $(x, y)$ . The receiving system consists of an echo RX and a direct-wave RX, where the heterodyne and in-phase receivers are used to simplify the system. The direct-wave RX is fixed at position  $(x_{ref}, y_{ref})$ , and the echo RX moves along a linear trajectory parallel to the  $X$ -axis. Let  $(x_{rx}, y_{rx})$  be a spatial sampling point of the echo receiver, and  $x_{rx} \in [-L_x/2, L_x/2]$ , where  $L_x$  denotes the observation aperture length in cross range (i.e., azimuth). The distance between the center of the imaging scene and that of the observation aperture is indicated by  $R_0$ . The target is assumed to be characterized by a reflectivity function  $\sigma(x, y)$ .

The TX emits SF signals, and its  $p$ th transmitted signal is

$$s_t(f_{tx,p}, t) = \cos(2\pi f_{tx,p}t + \varphi_{tx}) \quad (1)$$

where  $f_{tx,p}$  is the operating frequency at the transmitting end,  $f_{tx,p} = f_0 + (p-1)\Delta f$ ,  $f_0$  and  $\Delta f$  denote the start frequency and the frequency step, respectively,  $p = 1, 2, \dots, P$ .  $\varphi_{tx}$  denotes the initial phase induced by the local transmitter.

Let  $s_{rx}(x_{tx}, f_{tx,p}, t)$  represent the response at the echo receiver measured over a 1-D aperture (characterized by  $x_{tx}$ ).  $s_{rx}(x_{tx}, f_{tx,p}, t)$  is a superposition of each point on the target

multiplied by the bistatic round-trip phase to that point

$$s_{\text{rx}}(x_{\text{rx}}, f_{\text{tx},p}, t) = \iint_{(x,y)} \sigma(x,y) s_t(f_{\text{tx},p}, t - \tau_{\text{tx}}(x,y) - \tau_{\text{rx}}(x,y)) dx dy \quad (2)$$

where  $\tau_{\text{tx}}(x,y)$  and  $\tau_{\text{rx}}(x,y)$  indicate the time delay contributed by the transmitter and the echo receiver, respectively. Specifically, they are of the following form:

$$\begin{aligned} \tau_{\text{tx}}(x,y) &= \frac{R_{\text{tx}}(x,y)}{c} = \frac{\sqrt{(x_{\text{tx}} - x)^2 + (y_{\text{tx}} - y)^2}}{c} \\ \tau_{\text{rx}}(x,y) &= \frac{R_{\text{rx}}(x,y)}{c} = \frac{\sqrt{(x_{\text{rx}} - x)^2 + (y_{\text{rx}} - y)^2}}{c} \end{aligned} \quad (3)$$

where  $R_{\text{tx}}(x,y)$  and  $R_{\text{rx}}(x,y)$  are the range history between the TX and the target and that between the echo RX and the target, respectively, and  $c$  is the wave propagation velocity.

Similarly, the received signal at the direct-wave receiver is

$$s_{\text{ref}}(f_{\text{tx},p}, t) = s_t(f_{\text{tx},p}, t - \tau_{\text{ref}}) \quad (4)$$

where  $\tau_{\text{ref}}$  denotes the time delay induced by the direct-wave receiver.  $\tau_{\text{ref}} = \frac{R_{\text{ref}}}{c}$  is a constant in the current case because of the known and fixed positions of the transmitter and the direct-wave receiver, and  $R_{\text{ref}} = \sqrt{(x_{\text{ref}} - x_{\text{tx}})^2 + (y_{\text{ref}} - y_{\text{tx}})^2}$ .

Both the heterodyne and in-phase receivers are assumed to share the same local oscillator (LO). Therefore, the local signal corresponding to the  $p$ th transmitted SF signal at both the receivers can be written as

$$s_r(f_{\text{tx},p}, t) = \cos(2\pi f_{\text{tx},p} t + \varphi_{\text{tx}}) \quad (5)$$

where  $f_{\text{tx},p}$  and  $\varphi_{\text{tx}}$  denote the  $p$ th local frequency and the initial phase, respectively, and are different from  $f_{\text{tx},p}$  and  $\varphi_{\text{tx}}$ .

Therefore, after the heterodyne receiving, the in-phase intermediate frequency (IF) output of the echo receiver by combing (2) and (5) can be expressed as

$$\begin{aligned} s_{\text{IF,rx}}(x_{\text{rx}}, f_{\text{tx},p}, f_{\text{IF},p}, t) &= \text{LP} \{ s_{\text{rx}}(x_{\text{rx}}, f_{\text{tx},p}, t) s_r(f_{\text{tx},p}, t) \} \\ &= \iint_{(x,y)} \sigma(x,y) \\ &\quad \times \cos(\phi(x_{\text{rx}}, f_{\text{tx},p}, f_{\text{IF},p})) dx dy \\ \phi(x_{\text{rx}}, f_{\text{tx},p}, f_{\text{IF},p}) &= 2\pi f_{\text{IF},p} t + (\varphi_{\text{tx}} - \varphi_{\text{rx}}) \\ &\quad - 2\pi f_{\text{tx},p} (\tau_{\text{tx}}(x,y) + \tau_{\text{rx}}(x,y)) \end{aligned} \quad (6)$$

where the operator  $\text{LP}\{\cdot\}$  denotes the lowpass filter and is used to express the procedure of heterodyne processing for simplicity, and  $f_{\text{IF},p} = f_{\text{tx},p} - f_{\text{rx},p}$ . In general, a heterodyne receiver outputs a fixed IF when there is frequency synchronization. Here, we use  $f_{\text{IF},p}$  to indicate the possible frequency mismatch between the transmitter and the receivers.

Similarly, the in-phase IF output of the direct-wave receiver can be written as

$$\begin{aligned} s_{\text{IF,ref}}(f_{\text{tx},p}, f_{\text{IF},p}, t) \\ &= \text{LP} \{ s_{\text{ref}}(f_{\text{tx},p}, t) s_r(f_{\text{tx},p}, t) \} \\ &= \cos(f_{\text{IF},p} t + (\varphi_{\text{tx}} - \varphi_{\text{rx}}) - f_{\text{tx},p} \tau_{\text{ref}}). \end{aligned} \quad (7)$$

It is obvious to see from (6) that the terms of  $\varphi_{\text{tx}} - \varphi_{\text{rx}}$  and  $f_{\text{IF},p}$  imply the existence of synchronization problem. Benefit from the high coherence between the IF output of the echo RX [i.e., (6)] and that of the direct-wave RX [i.e., (7)], it is possible to solve the synchronization problem mathematically.

### B. Signal Model for Near-Field THz BiSAR Imaging

Although many progresses have been made based on monostatic SAR for THz near-field imaging [5]–[8], the situation is slightly more complex in the bistatic case. In contrast to the same range history in monostatic system, the out-coming range history contributed from transmitter and receiver in bistatic system is different. This difference between the monostatic and bistatic system makes their involved signal postprocessing for focusing inherently different [23]. Besides, although BiSAR is well known for the far-field applications in traditional microwave band, e.g., [12], [17], [23], the plane-wave assumption for far field is not suitable for the near-field case with spherical wavefront. Therefore, it can be inferred that designing BiSAR missions for THz near-field imaging comes at the cost of an increased complexity with respect to the processing of BiSAR raw data to SAR images.

At first, the Hilbert transform is used to convert both the IF echo and IF direct wave to their complex forms. Such that (6) and (7) can be rewritten as

$$\begin{aligned} s_{\text{rx}}(x_{\text{rx}}, f_{\text{tx},p}, f_{\text{IF},p}, t) \\ &= \text{Hilbert} \{ s_{\text{IF,rx}}(x_{\text{rx}}, f_{\text{tx},p}, f_{\text{IF},p}, t) \} \\ &= \iint_{(x,y)} \sigma(x,y) \\ &\quad \times e^{j \left\{ 2\pi (f_{\text{IF},p} t - f_{\text{tx},p} (\tau_{\text{tx}}(x,y) + \tau_{\text{rx}}(x,y))) \right.} \\ &\quad \left. + (\varphi_{\text{tx}} - \varphi_{\text{rx}}) \right\} dx dy \end{aligned} \quad (8)$$

$$\begin{aligned} s_{\text{ref}}(f_{\text{tx},p}, f_{\text{IF},p}, t) &= \text{Hilbert} \{ s_{\text{IF,ref}}(f_{\text{tx},p}, f_{\text{IF},p}, t) \} \\ &= e^{j 2\pi (f_{\text{IF},p} t - f_{\text{tx},p} \tau_{\text{ref}}) + j (\varphi_{\text{tx}} - \varphi_{\text{rx}})} \end{aligned} \quad (9)$$

Therefore, the direct wave can be used as a matched filter. Through a conjugate multiplication between (8) and (9), we can have a more concise signal as

$$\begin{aligned} s(x_{\text{rx}}, k_p) &= s_{\text{rx}}(x_{\text{rx}}, f_{\text{tx},p}, f_{\text{IF},p}, t) s_{\text{ref}}^*(f_{\text{tx},p}, f_{\text{IF},p}, t) \\ &= \iint_{(x,y)} \sigma(x,y) e^{-j k_p (R_{\text{tx}}(x,y) + R_{\text{rx}}(x,y) - R_{\text{ref}})} dx dy \end{aligned} \quad (10)$$

where  $k_p = 2\pi f_{\text{tx},p}/c$  refers to the wave number corresponding to the  $p$ th frequency, and  $(\cdot)^*$  represents the conjugate operation.

From the comparison between (6) and (10), it is easy to see that the possibly existed synchronization problem is removed.

As to the THz near-field imaging problem, the exponential term in (10) represents a spherical wave emanating from  $(x, y)$ , the far-field assumption will not be valid here. Hence, we first make a FT of (10) along the observation aperture to turn (10) into the wavenumber domain; it gives

$$s(k_x, k_p) = \int_{x_{\text{rx}}} s(x_{\text{rx}}, k_p) e^{-jk_x x_{\text{rx}}} dx_{\text{rx}} \quad (11)$$

where  $k_x$  is the wavenumber component in  $X$  dimension.

Let the phase in (11) be  $\phi(x, y, x_{\text{rx}})$ , and  $\phi(x, y, x_{\text{rx}})$  is

$$\phi(x, y, x_{\text{rx}}) = -k_p (R_{\text{tx}}(x, y) + R_{\text{rx}}(x, y) - R_{\text{ref}}) - k_x x_{\text{tx}}. \quad (12)$$

According to the principle of stationary position method, the integral of (11) can get its nonzero value around  $x_{\text{rx}}^*$ , where  $x_{\text{rx}}^*$  satisfies

$$x_{\text{rx}}^* = \arg \left\{ \frac{\partial \phi(x, y, x_{\text{rx}})}{\partial x_{\text{rx}}} = 0 \right\}. \quad (13)$$

Therefore, substituting (12) into (13), we can get

$$x_{\text{rx}}^* = x - \frac{k_x}{\sqrt{k_p^2 - k_x^2}} (y - y_{\text{rx}}). \quad (14)$$

Furthermore, we make a first-order Taylor expansion of the term  $R_{\text{tx}}(x, y)$  around the center of the imaging scene at  $(x_0, y_0)$ , and we can have

$$\begin{aligned} R_{\text{tx}}(x, y) &= R_{\text{tx}}(x_0, y_0) + \frac{x_0 - x_{\text{tx}}}{R_{\text{tx}}(x_0, y_0)} (x - x_0) \\ &\quad + \frac{y_0 - y_{\text{tx}}}{R_{\text{tx}}(x_0, y_0)} (y - y_0) \end{aligned} \quad (15)$$

where  $R_{\text{tx}}(x_0, y_0) = \sqrt{(x_0 - x_{\text{tx}})^2 + (y_0 - y_{\text{tx}})^2}$ .

Substituting (14) and (15) back into (11) yields

$$\begin{aligned} s(k_x, k_p) &= s(x_{\text{rx}}^*, k_p) e^{-jk_x x_{\text{rx}}^*} \\ &= e^{j\phi_p} \iint_{(x,y)} \sigma(x, y) e^{-jk_x' x - k_y' y} dx dy \end{aligned} \quad (16)$$

where  $\phi_p$  is the phase constant independent of  $(x, y)$ ,  $k_x'$  and  $k_y'$  denote the adjusted wavenumber component in  $X$  dimension and  $Y$  dimension, respectively, and

$$\phi_p = k_p \left( \frac{x_{\text{tx}}^2}{\sqrt{x_{\text{tx}}^2 + R_0^2}} + R_{\text{ref}} \right) \quad (17)$$

$$\begin{aligned} k_x' &= k_x + \frac{x_0 - x_{\text{tx}}}{R_{\text{tx}}(x_0, y_0)} k_p \\ k_y' &= \sqrt{k_p^2 - k_x^2} + \frac{y_0 - y_{\text{tx}}}{R_{\text{tx}}(x_0, y_0)} k_p. \end{aligned} \quad (18)$$

Because of the independence between  $(x, y)$  and  $e^{j\phi_p}$ , this phase term can be eliminated easily by using the corresponding phase compensation factor, such that (16) can be further

expressed as

$$\begin{aligned} s(k_x', k_y') &= e^{-j\phi_p} s(k_x, k_p) \\ &= \iint_{(x,y)} \sigma(x, y) e^{-jk_x' x - k_y' y} dx dy \end{aligned} \quad (19)$$

So far, the analytical expression based on BiSAR for THz 2-D near-field imaging is obtained.

### III. CS-BASED IMAGING RECONSTRUCTION

Obviously, the signal in (19) represents that the reflectivity function of target  $\sigma(x, y)$  and the received echo in wavenumber domain  $s(k_x', k_y')$  satisfies 2-D FT. However, the nonuniform distribution of  $(k_x', k_y')$  in the wavenumber domain implies that adopting the direct 2-D inverse FT is not a highly efficient way. Then, in general, an additional interpolation based on  $(k_x', k_y')$  would be added to make a uniform approximation of  $s(k_x', k_y')$ . Due to the concerned SF waveform and 1-D spatial observation, the bistatic system suffers a serious drawback of long time of data acquisition, which depends on the time taken at each frequency, the number of total frequency points, and the number of spatially observation positions.

The recently introduced theory of CS allows the use of a subset of frequencies and spatial samples instead of their full sets to improve the measurement speed and to reduce the amount of measurements. However, a 2-D undersampling scheme in the frequency and spatial domains is adopted, the coupling nature of  $k_x'$  and  $k_y'$  shown in (18) implies these two dimensions inseparable. To avoid extra approximation errors in decoupling  $k_x'$  and  $k_y'$ , we convert this near-field 2-D imaging in (19) into a 1-D sparse reconstruction problem.

Letting  $L$  be the number of all the possible scatterers in the imaging scene, (19) can be straightforwardly expressed into a discrete form

$$s(k_x'(m), k_y'(p, m)) = \mathbf{a}^T(p, m) \boldsymbol{\sigma} + w(p, m) \quad (20)$$

where  $(\cdot)^T$  denotes the transpose operation,  $m$  denotes the index of 1-D spatially sampling position of the echo receiver,  $m = 1, \dots, M$ ,  $p$  is the index of the frequency of the SF waveform,  $p = 1, \dots, P$ ,  $\mathbf{a}(p, m)$  denotes the measurement vector at the  $p$ th frequency, and the  $m$ th observation position, and  $\boldsymbol{\sigma}$  denotes the unknown scattering vector,  $w(p, m)$  represents the noise term. Specifically,  $\mathbf{a}(p, m)$  and  $\boldsymbol{\sigma}$  are of the form as

$$\begin{aligned} \mathbf{a}(p, m) &= \left[ e^{-j \left\{ \begin{array}{l} k_x'(m) x_1 \\ + k_y'(p, m) y_1 \end{array} \right\}}, \dots, e^{-j \left\{ \begin{array}{l} k_x'(m) x_L \\ + k_y'(p, m) y_L \end{array} \right\}} \right]^T \\ \boldsymbol{\sigma} &= [\sigma(x_1, y_1), \dots, \sigma(x_L, y_L)]^T. \end{aligned}$$

Such that stacking all the samplings from frequency points and observation positions, we can have

$$\mathbf{s} = \mathbf{A} \boldsymbol{\sigma} + \mathbf{w} \quad (21)$$

where  $\mathbf{s} \in \mathbb{C}^{MP \times 1}$ ,  $\mathbf{A} \in \mathbb{C}^{MP \times L}$  and  $\mathbf{w} \in \mathbb{C}^{MP \times 1}$  denote the measurement vector, measurement matrix, and noise vector,



respectively, and

$$\begin{aligned} \mathbf{s} &= [\mathbf{s}_1^T, \dots, \mathbf{s}_P^T]^T \\ \mathbf{s}_p &= \begin{bmatrix} s(k'_x(1), k'_y(p, 1)) \\ \vdots \\ s(k'_x(M), k'_y(p, m)) \end{bmatrix} \\ \mathbf{A} &= [\mathbf{A}_1^T, \dots, \mathbf{A}_P^T]^T \\ \mathbf{A}_p &= [\mathbf{a}(p, 1), \dots, \mathbf{a}(p, m)]^T \\ \mathbf{w} &= [w(1, 1), \dots, w(p, m)]^T. \end{aligned} \quad (22)$$

The random selection of the observation position and frequency points is allowed. The solution to (21) is universally studied and lots of reconstruction algorithms are proposed for various applications [24]–[26]. Here, we resort to the maximum *a posteriori* (MAP) approach, and consider the elements of  $\mathbf{w}$  following independent identically distributed Gaussian distribution with zero expectation and  $\gamma$  variation, i.e.,  $\mathbf{w} \sim \mathcal{CN}(\mathbf{0}, \gamma \mathbf{I})$ . Such that the Bayesian model of (21) can be viewed as follows:

$$p_{\mathbf{w}}(\mathbf{y} | \boldsymbol{\sigma}, \gamma) = \frac{1}{(\pi\gamma)^{MP}} e^{-\frac{1}{\gamma} \|\mathbf{y} - \mathbf{A}\boldsymbol{\sigma}\|_2^2} \quad (23)$$

Then, we let Laplace prior be the sparse promoting prior for  $\boldsymbol{\sigma}$ , which is a widely used sparse prior in radar field [24], [25]. That is, the probability of  $\boldsymbol{\sigma}$  satisfies

$$p_{\boldsymbol{\sigma}}(\boldsymbol{\sigma}) \propto e^{-\|\boldsymbol{\sigma}\|_1} \quad (24)$$

where  $\|\cdot\|_1$  represents the  $l_1$  norm of a vector, i.e.,  $\|\boldsymbol{\sigma}\|_1 = \sum_{i=1}^L |\sigma_i|$ .

Based on (23) and (24), the estimate of  $\boldsymbol{\sigma}$  and  $\gamma$  can be obtained by the MAP approach

$$\max_{\boldsymbol{\sigma}, \gamma} p_{\mathbf{w}}(\mathbf{y} | \boldsymbol{\sigma}, \gamma) p_{\boldsymbol{\sigma}}(\boldsymbol{\sigma}). \quad (25)$$

Furthermore, by taking the negative logarithm of (25), the image reconstruction can be given by the following 1-D unconstrained optimization problem

$$\min_{\boldsymbol{\sigma} \in \mathbb{C}^{L \times 1}, \gamma} F(\boldsymbol{\sigma}, \gamma) = MP \log \gamma + \frac{1}{\gamma} \|\mathbf{A}\boldsymbol{\sigma} - \mathbf{s}\|_2^2 + \|\boldsymbol{\sigma}\|_1 \quad (26)$$

where  $F(\boldsymbol{\sigma}, \gamma)$  denotes the cost function.

Since there are no closed-form solutions for  $\boldsymbol{\sigma}$  and  $\gamma$ , we adopt an alternating iterative method to compute their MAPs-like estimates (see [26] for more information). The detailed steps of the CS-based reconstruction algorithm for THz BiSAR 2-D near-field imaging is shown in Algorithm 1.

#### IV. SIMULATION AND EXPERIMENT

The spatial sampling interval and the sampling interval in frequency domain based on the Nyquist theory, respectively, are approximated as

$$\Delta x^* \approx \frac{\lambda}{2} \quad \Delta f^* \approx \frac{c}{2R_{\max}} \quad (27)$$

---

#### Algorithm 1: CS-based imaging algorithm for THz BiSAR near-field imaging.

---

##### Input:

Receive IF echo and IF direct-wave signal over the frequency and spatial domain,  $s_{\text{IF,rx}}(f_{\text{tx},p}, f_{\text{IF},p}, x_{\text{rx}}, t)$  and  $s_{\text{IF,ref}}(f_{\text{tx},p}, f_{\text{IF},p}, t)$ ;

##### Output:

- 1: Take the Hilbert transform on IF signal  $s_{\text{IF,rx}}$  and  $s_{\text{IF,ref}}$  to get their complex forms, denoted as  $s_{\text{rx}}(f_{\text{tx},p}, f_{\text{IF},p}, x_{\text{rx}}, t)$  and  $s_{\text{ref}}(f_{\text{tx},p}, f_{\text{IF},p}, t)$ , respectively.
- 2: Apply a conjugate multiplication over  $s_{\text{rx}}$  and  $s_{\text{ref}}$  to remove the possible synchronization errors.

$$s(x_{\text{rx}}, k_p) = s_{\text{rx}}(x_{\text{rx}}, f_{\text{tx},p}, f_{\text{IF},p}, t) s_{\text{ref}}^*(f_{\text{tx},p}, f_{\text{IF},p}, t)$$

- 3: Take the spatial 1-D FT of  $s(x_{\text{rx}}, k_p)$  to form the angular spectrum at each frequency.

$$s(k_x, k_p) = \int_{x_{\text{rx}}} s(x_{\text{rx}}, k_p) e^{-jk_x x_{\text{rx}}} dx_{\text{rx}}$$

- 4: Apply a series of phase compensation functions to the angular spectrums.

$$s(k'_x, k'_y) = e^{-j\phi_p} s(k_x, k_p)$$

where  $\phi_p$  is given in (17). Then, we can obtain its discrete form by stacking all the samples

$$\mathbf{s} = \mathbf{A}\boldsymbol{\sigma} + \mathbf{w}$$

where the detail forms of  $\mathbf{s}$ ,  $\mathbf{A}$ ,  $\boldsymbol{\sigma}$ , and  $\mathbf{w}$  are shown in (22), respectively.

- 5: Initialize the noise level  $\gamma^{(0)}$ , the initial value  $\boldsymbol{\sigma}^{(0)}$ , and set the iteration step  $q = 0$ .
- 6: Argument  $q = q + 1$ .
- 7: Update the scattering vector  $\boldsymbol{\sigma}$ .

$$\boldsymbol{\sigma}^{(q)} = \left[ \mathbf{A}^H \mathbf{A} + \gamma^{(q-1)} (\boldsymbol{\Lambda}^{(q-1)})^{-1} \right]^{-1} \mathbf{A}^H \mathbf{y}$$

where  $\boldsymbol{\Lambda} = \text{diag} \{ [|\sigma_1|, \dots, |\sigma_L|]^T \}$

- 8: Update the noise level  $\gamma$ .

$$\gamma^{(q)} = \frac{1}{MP} \left\| \mathbf{y} - \mathbf{A}\boldsymbol{\sigma}^{(q)} \right\|_2^2$$

- 9: Stop the algorithm if  $F(\boldsymbol{\sigma}^{(q)}, \gamma^{(q)})$  meets with the stop condition; otherwise, go back to step 6 and continue.
  - 10: **return**  $\hat{\boldsymbol{\sigma}} = \boldsymbol{\sigma}^{(q)}$ .
- 

where  $\lambda$  denotes the minimum wavelength of the transmitted signal and  $R_{\max}$  is the maximum range of the image scene.

The theoretical resolutions in cross range, denoted as  $\rho_x$ , and in range dimension, denoted as  $\rho_y$ , are, respectively, calculated as

$$\rho_x = \frac{c\sqrt{4R_0^2 + L_x^2}}{2f_{\text{tx},0}L_x} \quad \rho_y = \frac{c}{2B} \quad (28)$$

TABLE I  
DETAILED SYSTEM PARAMETERS

Parameters	Variable	Value
Transmitting start frequency	$f_{tx,0}$	178 GHz
Receiving start frequency	$f_{rx,0}$	178.1 GHz
Bandwidth	$P \cdot \Delta f$	10 GHz
Aperture length	$L_x$	30 cm
Position of TX	$(x_{tx}, y_{tx})$	(-25, 0) cm
Position of the direct-wave RX	$(x_{ref}, y_{ref})$	(-20, 35) cm
The center of the imaging scene	$(x_0, y_0)$	(0, 35) cm
Position of the echo RX	$x_{rx}$	[-15, 15] cm
	$y_{rx}$	0 cm
Spatial sampling interval(*)	$\Delta x^*$	0.8 mm
Frequency sampling interval(*)	$\Delta f^*$	375 MHz
Theoretical azimuth resolution	$\rho_x$	2.1 mm
Theoretical range resolution	$\rho_y$	15 mm
Signal-to-noise	SNR	5 dB

### A. Imaging Based on Simulations

The conventional FT algorithm is taken as a comparison with our proposed method. And here we take into account the undersampling with uniform interval.

According to the geometry shown in Fig. 1, the size of imaging scene is [20, 50] cm  $\times$  [-20, 20] cm, and the detail parameters are collected in Table I. Thereby, according to the Nyquist theory, when  $\Delta x = \Delta x^*$  and  $\Delta f = \Delta f^*$ , there are about 375 spatial samples in a 30-cm-long linear trajectory and approximately 30 frequency-domain samples over 10 GHz bandwidth. The total size of the full data set is  $375 \times 30$ .

It is obvious from Fig. 2(a) and (b) that FT-based algorithm can yield good imaging when given sufficient data, while the decreased amount of data seriously deteriorates its performance. However, Fig. 2(c) shows that the proposed algorithm is still able to achieve imaging with low-side lobe when the amount of data is only 12.5% of that required by the FT algorithm.

Furthermore, under the assumption that all the scatterers are exactly located on the discretized grids of the imaging scene, the limit resolution of the proposed algorithm in cross-range and range dimension for noiseless case is examined, respectively. Shown in Fig. 3, it is apparent that both the algorithms can accurately reconstruct the scatterers when the distance between two scatterers is greater than the theoretical resolution.

### B. Imaging Based on Experiments

To perform proof-of-principle experiments, a prototype imager is developed in the 0.178–0.188 THz band. The experimental scenario is given in Fig. 4, where there is a SF transmitter with a fixed position, one heterodyne and in-phase echo receiver mounted on a linear-motion platform to make the spatial observation, another receiver with the same configuration to receive direct wave with a fixed position, and an oscilloscope as the signal acquisition module. Specifically, the transmitter and two receivers are externally equipped by different  $Ku$ -band LO, respectively. Obviously, the synchronization is not guaranteed between the transmitter and receivers, while the two receivers are synchronized by a high-precision divider with phase

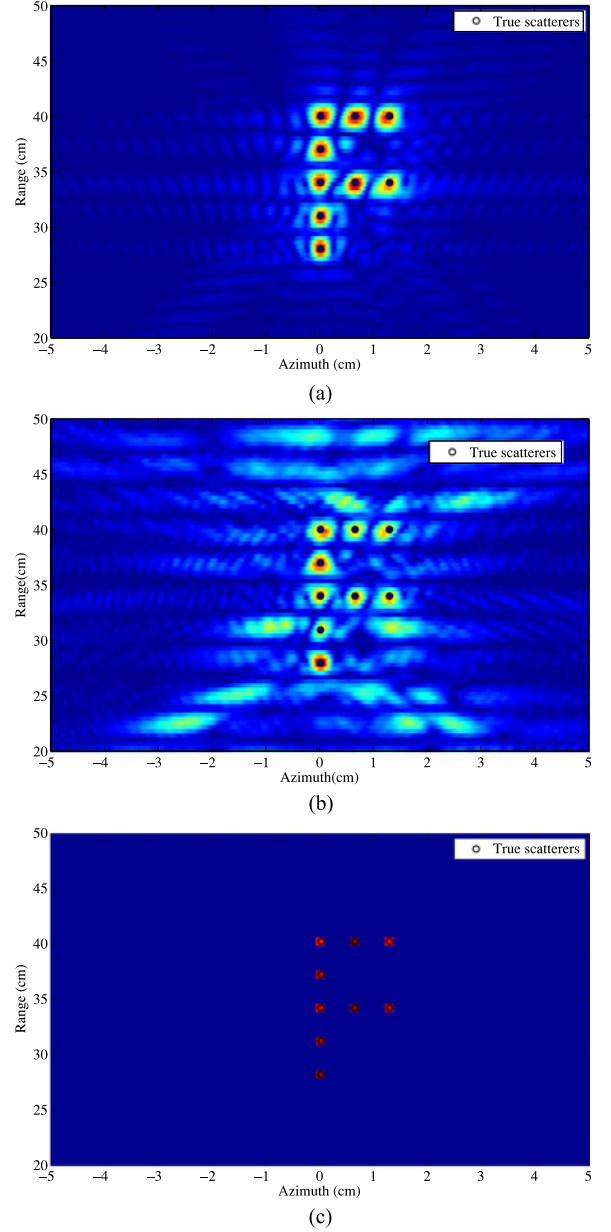


Fig. 2. Imaging performance. (a) FT algorithm with full-sampling ( $\Delta x = \Delta x^*$ ,  $\Delta f = \Delta f^*$ ), (b) FT algorithm with down-sampling ( $\Delta x = 4\Delta x^*$ ,  $\Delta f = 2\Delta f^*$ ), (c) Proposed algorithm with down-sampling ( $\Delta x = 4\Delta x^*$ ,  $\Delta f = 2\Delta f^*$ ).

matching. The advanced oscilloscope works at a two-channel mode to acquire the echo and direct wave synchronously. The involved parameters are set the same as Table I shows. The involved antennas are of the same parameters, where the gain is 24 dB and the 3 dB beamwidth is about  $15^\circ$ . The data set is acquired according to the undersampling condition as  $\Delta x = 4\Delta x^*$  and  $\Delta f = 2\Delta f^*$ , which is only 12.5% amount of data compared with that required by an FT-based algorithm.

The simplified BiSAR imaging procedure for THz near-field imaging is presented in Fig. 5. First, there are two metal cylinders of the same range as the objects under test, as shown in Fig. 6(a). The diameter of each cylinder is 1.3 cm and the distance between two cylinders is 3 cm in the cross-range

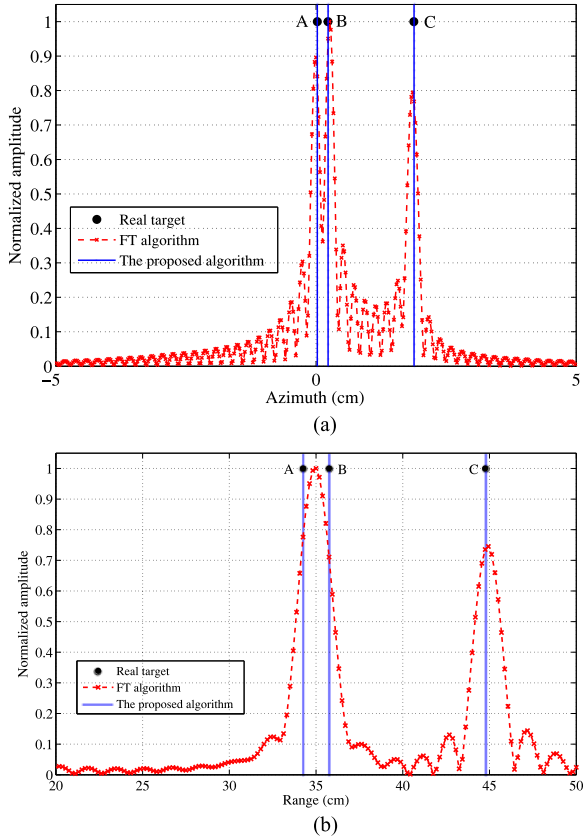


Fig. 3. Ideal resolution performance, where the sampling condition of FT algorithm is set as  $\Delta f = \Delta f^*$ ,  $\Delta x = \Delta x^*$ , and that of the proposed algorithm is set as  $\Delta f = 2\Delta f^*$ ,  $\Delta x = 4\Delta x^*$ . (a) Azimuth resolution,  $|x_A - x_B| = \rho_x$ ,  $|x_B - x_C| = 10\rho_x$ ,  $y_A = y_B = y_C$ . (b) Range resolution,  $|y_A - y_B| = \rho_y$ ,  $|y_B - y_C| = 10\rho_y$ ,  $x_A = x_B = x_C$ .

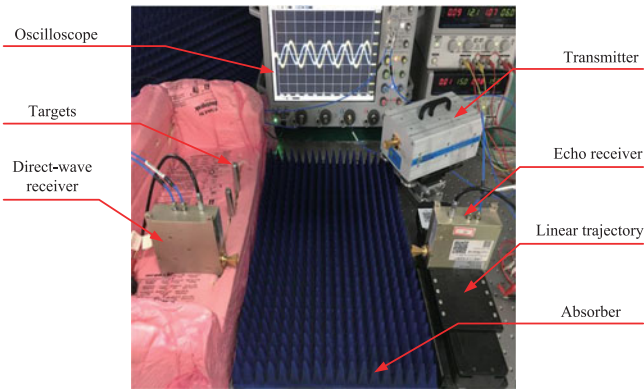


Fig. 4. Photograph of the THz BiSAR experimental system.

dimension. Then, there are two metal blocks with the same width of 4 cm as the objects under test, as shown in Fig. 7(a). They are placed in the same range and are 2 cm apart from each other in the cross-range dimension. The measurements are stacked as (21) requires. Figs. 6(b) and 7(b) demonstrate that the targets can be well resolved by the proposed algorithm. Furthermore, the case of multiple targets is examined, shown in Fig. 8(a), and the diameter of each cylinder is still 1.3 cm. The 2-D imaging result is shown in Fig. 8(b), where the respective center of each true cylinder is expressed by a red round. It is seen that the

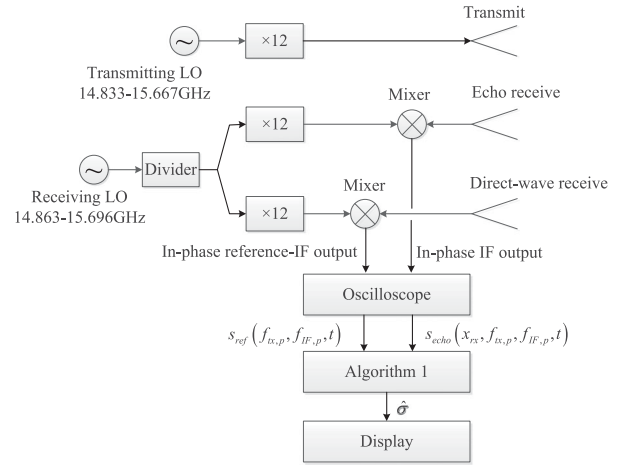
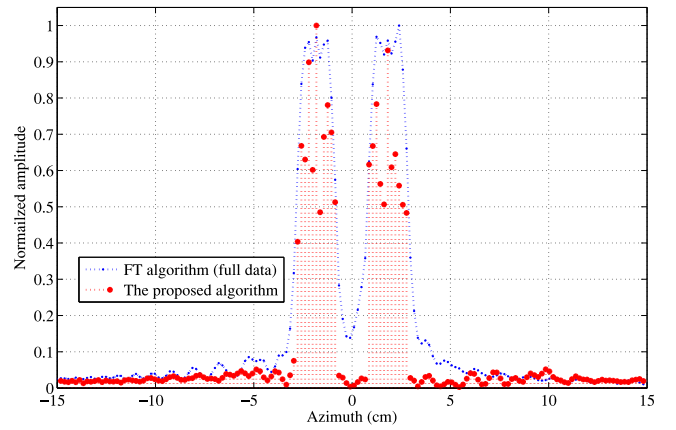


Fig. 5. Simplified bistatic THz SAR imaging system.



(a)



(b)

Fig. 6. Imaging result for two metal cylinders. (a) Photograph of two metal cylinders. (b) Imaging result.

proposed algorithm can clearly identify the targets with such few measurements. Here, it should be noted that the relatively high sidelobes at this time would be caused by the multipath effect among those metal targets. Then, considering the transmitter position at  $(-25, 0)$  cm and the limit beamwidth of the adopted antenna, it is reasonable to have that the farthest cylinder from the transmitter is reconstructed with a lowest amplitude.

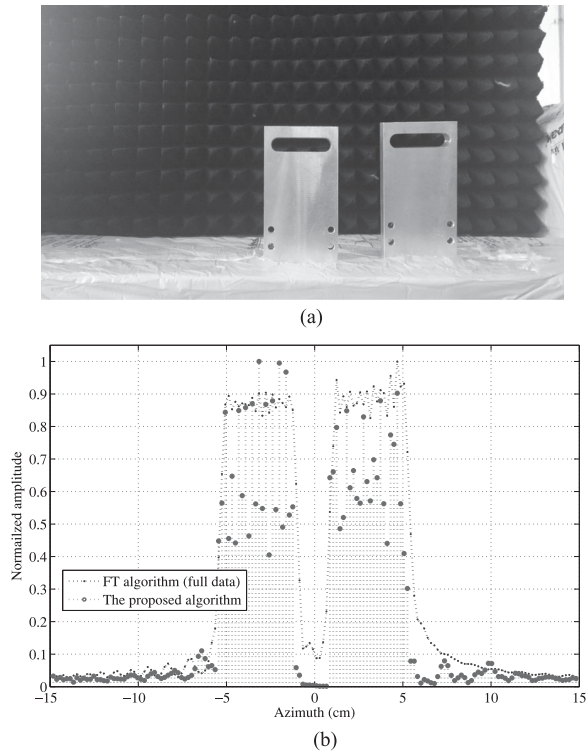


Fig. 7. Imaging result for two metal blocks. (a) Photograph of two metal blocks. (b) Imaging result.

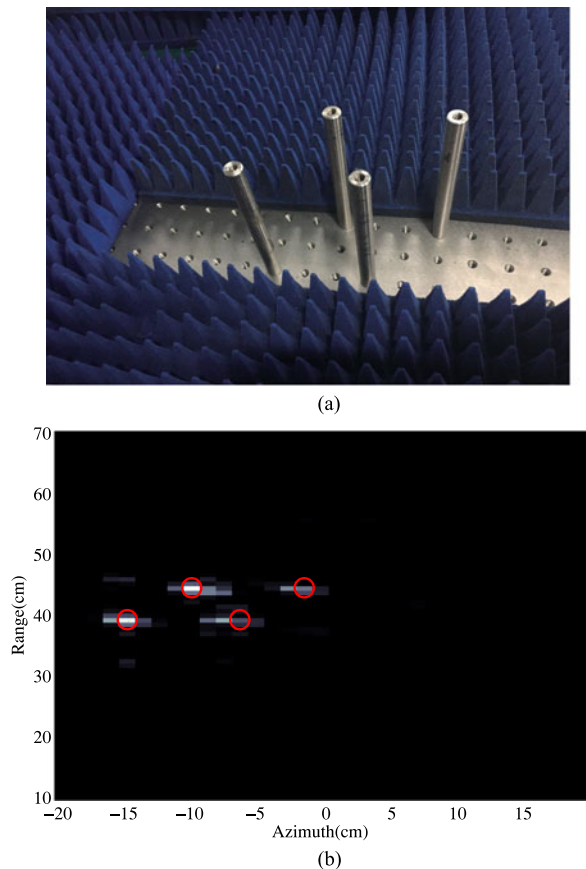


Fig. 8. Imaging result for multiple metal cylinders. (a) Photograph of multiple cylinders. (b) Imaging result.

In a nutshell, the experiments demonstrate that the proposed algorithm can achieve good imaging with the reduced scale of measurements. It thus shows its feasibility in practical application, especially to speed up the signal acquisition and to reduce the computational complexity.

## V. CONCLUSION

This paper has demonstrated a compact BiSAR geometry for THz near-field imaging. The bistatic configuration is taken to avoid the difficulty in achieving great transceiver isolation when applying monostatic SAR into THz band. The system is simplified by adopting in-phase receiving scheme. The two-receiver configuration makes the potential synchronization problem be overcome through a mathematical way. Motivated by CS, the common  $l_1$ -norm-based sparse imaging algorithm is introduced and demonstrated to achieve high-performance imaging when both the spatial domain and frequency domain are undersampled. Compared with the conventional FT-based algorithm, the CS-based imaging method can work well with dramatically reduced amount of measurements. Simulations and proof-of-principle experiments are both performed in the 0.178–0.188 THz band, which indicate the feasibility of BiSAR scheme and the practicability of CS-based sparse reconstruction for applications in THz near-field imaging.

## REFERENCES

- [1] D. Arnone, C. Ciesla, and M. Pepper, "Terahertz imaging comes into view," *Phys. World*, vol. 13, no. 4, pp. 35–40, 2000.
- [2] R. Appleby and H. B. Wallace, "Standoff detection of weapons and contraband in the 100 GHz to 1 THz region," *IEEE Trans. Antennas Propag.*, vol. 55, no. 11, pp. 2944–2956, Nov. 2007.
- [3] K. B. Cooper *et al.*, "THz imaging radar for standoff personnel screening," *IEEE Trans. THz Sci. Technol.*, vol. 1, no. 1, pp. 169–182, Sep. 2011.
- [4] S. S. Dhillon *et al.*, "The 2017 terahertz science and technology roadmap," *J. Phys. D Appl. Phys.*, vol. 50, no. 4, 2017, Art. no. 043001.
- [5] D. M. Sheen, D. L. McMakin, and T. E. Hall, "Three-dimensional millimeter-wave imaging for concealed weapon detection," *IEEE Trans. Microw. Theory Techn.*, vol. 49, no. 9, pp. 1581–1592, Sep. 2001.
- [6] P. Corredoura, Z. Baharav, and G. Lee, "Millimeter-wave imaging system for personnel screening: Scanning  $10^7$  points a second and using no moving parts," in *Proc. Defense Security Symp.*, 2006, pp. 62110B-1–62110B-8.
- [7] K. B. Cooper, R. J. Dengler, N. Llombart, B. Thomas, G. Chattopadhyay, and P. H. Siegel, "Thz imaging radar for standoff personnel screening," *IEEE Trans. THz Sci. Technol.*, vol. 1, no. 1, pp. 169–182, Sep. 2011.
- [8] S. Li *et al.*, "Study of terahertz superresolution imaging scheme with real-time capability based on frequency scanning antenna," *IEEE Trans. THz Sci. Technol.*, vol. 6, no. 3, pp. 451–463, May 2016.
- [9] S. S. Ahmed, A. Genghammer, A. Schiessl, and L. P. Schmidt, "Fully electronic E-band personnel imager of 2 m<sup>2</sup> aperture based on a multi-static architecture," *IEEE Trans. Microwave Theory Techn.*, vol. 61, no. 1, pp. 651–657, Jan. 2013.
- [10] R. Wang, B. Deng, Y. Qin, and H. Wang, "Bistatic terahertz radar azimuth-elevation imaging based on compressed sensing," *IEEE Trans. THz Sci. Technol.*, vol. 4, no. 6, pp. 702–713, Nov. 2014.
- [11] B. Baccouche *et al.*, "3D terahertz imaging with sparse multistatic line arrays," *IEEE J. Sel. Topics Quantum Electron.*, vol. 23, no. 4, 2017, Art. no. 8501411.
- [12] F. Comblet, A. Khenchaf, A. Baussard, and F. Pellen, "Bistatic synthetic aperture radar imaging: Theory, simulations, and validations," *IEEE Trans. Antennas Propag.*, vol. 54, no. 11, pp. 3529–3540, Nov. 2006.
- [13] I. Walterscheid, J. H. G. Ender, A. R. Brenner, and O. Loffeld, "Bistatic SAR processing and experiments," *IEEE Trans. Geosci. Remote Sens.*, vol. 44, no. 10, pp. 2710–2717, Oct. 2006.



- [14] R. J. Burkholder, L. J. Gupta, and J. T. Johnson, "Comparison of monostatic and bistatic radar images," *IEEE Antennas Propag. Mag.*, vol. 45, no. 3, pp. 41–50, Jun. 2003.
- [15] A. A. Danylov *et al.*, "Terahertz inverse synthetic aperture radar (ISAR) imaging with a quantum cascade laser transmitter," *Opt. Express*, vol. 18, no. 15, pp. 16 264–72, 2010.
- [16] J. Moll, P. Schops, and V. Krozer, "Towards three-dimensional millimeter-wave radar with the bistatic fast-factorized back-projection algorithm—Potential and limitations," *IEEE Trans. THz Sci. Technol.*, vol. 2, no. 4, pp. 432–440, Jul. 2012.
- [17] M. Antoniou, M. Cherniakov, and C. Hu, "Space-surface bistatic SAR image formation algorithms," *IEEE Trans. Geosci. Remote Sens.*, vol. 47, no. 6, pp. 1827–1843, Jun. 2009.
- [18] M. Zhang *et al.*, "A synchronization algorithm for spaceborne/stationary BiSAR imaging based on contrast optimization with direct signal from radar satellite," *IEEE Trans. Geosci. Remote Sens.*, vol. 54, no. 4, pp. 1977–1989, Apr. 2016.
- [19] D. L. Donoho, "Compressed sensing," *IEEE Trans. Inf. Theory*, vol. 52, no. 4, pp. 1289–1306, Apr. 2006.
- [20] M. Lustig, D. Donoho, and J. M. Pauly, "Sparse MRI: The application of compressed sensing for rapid MR imaging," *Magn. Reson. Med.*, vol. 58, no. 6, pp. 1182–1195, 2007.
- [21] M. A. Herman and T. Strohmer, "High-resolution radar via compressed sensing," *IEEE Trans. Signal Process.*, vol. 57, no. 6, pp. 2275–2284, Jun. 2009.
- [22] C. R. Berger, S. Zhou, J. C. Preisig, and P. Willett, "Sparse channel estimation for multicarrier underwater acoustic communication: From subspace methods to compressed sensing," *IEEE Trans. Signal Process.*, vol. 58, no. 3, pp. 1708–1721, Mar. 2010.
- [23] Y. L. Neo, F. Wong, and I. G. Cumming, "A two-dimensional spectrum for bistatic SAR processing using series reversion," *IEEE Geosci. Remote Sens. Lett.*, vol. 4, no. 1, pp. 93–96, Jan. 2007.
- [24] G. Xu, M. Xing, L. Zhang, Y. Liu, and Y. Li, "Bayesian inverse synthetic aperture radar imaging," *IEEE Geosci. Remote Sens. Lett.*, vol. 8, no. 6, pp. 1150–1154, Nov. 2011.
- [25] H. Liu, J. Bo, H. Liu, and Z. Bao, "Superresolution ISAR imaging based on sparse Bayesian learning," *IEEE Trans. Geosci. Remote Sens.*, vol. 52, no. 8, pp. 5005–5013, Aug. 2014.
- [26] X. Tan, W. Roberts, J. Li, and P. Stoica, "Sparse learning via iterative minimization with application to MIMO radar imaging," *IEEE Trans. Signal Process.*, vol. 59, no. 3, pp. 1088–1101, Mar. 2011.



**Yangyang Ye** received the bachelor's degree in communication engineering from the Nanjing University of Science and Technology, Nanjing, China, in 2015. He is currently working toward the master's degree in signal and information processing at the University of Shanghai for Science and Technology, Shanghai, China.

His research interests include THz near-field imaging, THz image processing, and imaging geometry design.



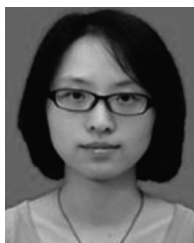
**Guoyao Ye** is currently working toward the degree at the Terahertz Technology Innovation Research Institute, University of Shanghai for Science and Technology (USST), Shanghai, China.

His research interests include millimeter-wave and terahertz technology, especially THz-inverse synthetic-aperture radar imaging and THz-SAR/ISAR image enhancement.



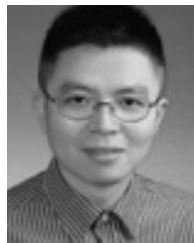
**Xiwang Wang** received the bachelor's degree in electronic engineering from the University of Shanghai for Science and Technology (USST), Shanghai, China, in 2016. He is currently working toward the master's degree at the Terahertz Technology Innovation Research Institute, USST.

His research interests include THz-based material identification technology, THz polarimetric detection and decomposition, etc.



**Li Ding** received the bachelor's and master's degrees from the University of Electronic Science and Technology of China, Chengdu, China, in 2008, the Ph.D. degree from the University of Science and Technology of China, Hefei, China, in 2011.

She is currently an Assistant Professor with the University of Shanghai for Science and Technology, Shanghai, China. Her research interests include millimeter-wave and terahertz-wave technology, especially with the applications to target detection and imaging.



**Yiming Zhu** received the bachelor's degree in applied physics and Ph.D. degree in electronic engineering Shanghai Jiao Tong University, Shanghai, China, in 2002 and 2008, respectively.

In 2003, he was an Assistant Researcher with the Research Center for Advanced Science and Technology, University of Tokyo, Tokyo, Japan. He is currently a Professor with the University of Shanghai for Science and Technology, Shanghai, China. His research interests include ultrafast optics, ultrafast electronics, and terahertz technology.